A&A 405, 415–424 (2003)
DOI: 10.1051/0004-6361:20030614


Astronomy & Astrophysics

# LBQS 1429-0053: A binary quasar rather than a lensed quasar⋆

C. Faure[1,3], D. Alloin[1], S. Gras[1], F. Courbin[2], J.-P. Kneib[3,4], and P. Hudelot[3]

[1] European Southern Observatory, Alonso de Cordova 3107, Casilla 19001, Santiago 19, Chile
[2] Institut d'Astrophysique et de Géophysique, Faculté des Sciences, Université de Liège, Allée du 6 août, 17, B5C, Liège 1, Belgium
[3] Observatoire Midi−Pyrénées, UMR 5572, 14 avenue Edouard Belin, 31400 Toulouse, France
[4] Caltech Astronomy Department, Mail Code 105-24, Pasadena, CA 91125, USA

Received 20 December 2002 / Accepted 27 March 2003

**Abstract.** Very deep ESO/VLT FORS1 and ISAAC images, as well as HST NICMOS2 data are used to infer the nature of the quasar pair LBQS 1429-0053 A and B, either a binary quasar or a doubly-imaged lensed quasar. Direct search of a putative lensing galaxy is unsuccessful down to $R = 27$, $J = 24$, $Ks = 22.5$ and $H = 22.5$. Moreover, no galaxy overdensity close to the quasar pair is found. A weak shear analysis of the FORS1 $R$-band $6.8' \times 6.8'$ field also fails at detecting any concentration of dark matter more massive than $\sigma = 500$ km s$^{-1}$ and weakens the hypothesis of a dark lens. The only sign of a possible lens consists in a group of 5 objects having colors consistent with galaxies at $z \sim 1$, within a radius of $5''$ from the quasar pair. Considering this group as the lensing potential does not allow to reproduce the image position and flux ratio of LBQS 1429-0053 A and B. Our deep $R$-band image shows a blue, previously unknown, extended object at the position of LBQS 1429-0053 A, which is consistent with either being the lensed quasar A host, or being an intervening galaxy at lower redshift. Unless future very deep optical images demonstrate that this object is actually the lensed host of LBQS 1429-0053, we conclude that there is very little evidence for LBQS 1429-0053 being lensed. Therefore, we are led to declare LBQS 1429-0053 A and B a genuine binary quasar.

**Key words.** galaxies: clusters: general – gravitational lensing – quasar: individual: LBQS 1429-0053

## 1. Introduction

Doubly-imaged quasars were initially thought to be the easiest cases of gravitational lenses to interpret and model. The first discovered gravitational lens was indeed a double, Q 0957+561 (Walsh et al. 1979), with an image separation of $6''$. Yet, doubles are just as challenging to interpret as more complex image configurations. In addition, while the lensing interpretation is often invoked to explain quasar pairs, they could well be genuine binary quasars. As a matter of fact, about 14 quasar pairs with large angular separation (larger than $3''$) remain inconclusive cases to whether they are binary quasars or doubly-imaged lensed quasars. The quasar pair LBQS 1429-0053 is one of them (Hewett et al. 1989).

The long-standing question whether some of the observed quasar pairs are doubly-imaged lensed quasars or genuine binary quasars has been revived through recent discussions by e.g. Mortlock et al. (1999), Kochanek et al. (1999) and Peng et al. (1999). This question bears important cosmological implications. If an observed pair is a genuine binary quasar, the spectral similarity of the two components is an exciting feature telling us about the formation and feeding of massive black holes. If it is a doubly-imaged quasar, the absence of a detectable luminous lens is pushing forward the idea of dark lenses. Understanding the nature of double quasars is therefore of great importance.

Recently, Peng et al. (1999) have touched upon this problem, studying the nature of the quasar pair Q 1634+267. They do not detect any lensing galaxy, but, because of the close similarity of the quasar spectra, they still envisage the dark lens hypothesis. To confirm their hypothesis, Peng et al. (1999) suggest to measure the light curves of both quasars, as they should be almost identical in case of gravitational lensing. Another complementary way is to try to directly detect a large mass concentration, even dark, along the line of sight, by performing a weak lensing analysis or deep X-ray observations.

The quasar pair LBQS 1429-0053 A and B (component A: $\alpha$ = 14:32:29.3, $\delta$ = −01:06:16, J2000) was first observed in spectroscopic mode at the MMT (Hewett et al. 1989). The spectra of LBQS 1429-0053 A and LBQS 1429-0053 B were found to be very similar, showing the emission lines and blends of Ly$\alpha$-NV, SiIV-OIV, CIV and CIII], very common in quasar spectra. An additional spectrum of LBQS 1429-0053 A reveals strong MgII emission line (Mortlock et al. 1999). The quasar

*Send offprint requests to*: C. Faure, e-mail: cfaure@eso.org

⋆ Based on observations obtained with VLT/ANTU at ESO-Paranal Observatory (program 67.A-0502) and with the Hubble Space Telescope, operated by NASA.

redshift is $z = 2.076$. The separation of the two components is large, 5.1″. A search for a putative lensing object, on an image obtained at CFHT down to $R = 24.5$, remained unsuccessful. But this does not rule out the presence of a lens (see for example the case of the Cloverleaf, Kneib et al. 1998).

LBQS 1429-0053 has been classified as an $O^2$ pair by Kochanek et al. (1999), meaning that both quasars are radio faint. According to the statistical analysis presented in that paper, the $O^2$ property does not allow to conclude whether the quasar pair is a lensed system or a genuine binary quasar. Moreover, in the analysis of Mortlock et al. (1999), the nature of LBQS 1429-0053 could not be established either, with any certainty: according to these authors, the degree of similarity between the spectra from LBQS 1429-0053 A and LBQS 1429-0053 B, is consistent with this system being either a lensed doubly-imaged quasar or a binary quasar.

If LBQS 1429-0053 is actually lensed, the spectral differences between A and B could still be attributed to a number of effects: (a) to microlensing by stars in the lensing galaxy, (b) to absorption by dust in the lens, or (c) to the long time-delay expected for the system and implying that images A and B could correspond to the quasar seen at two different epochs, hence possibly in a different state of activity. A tentative model of the lensing object was proposed by Hewett et al. (1989), but was largely under-constrained. Assuming that LBQS 1429-0053 is lensed, two models were considered. The first model had a deflector (point mass) of cluster mass ($\mathcal{M} \sim 1 \times 10^{13}\,\mathcal{M}_\odot$), at the redshift of one of the two observed MgII absorption system, $z_l \sim 1.5$. The second model, with $z_l \sim 0.6$, implied a deflector with an extremely high mass-to-light ratio ($\mathcal{M} \sim 2 \times 10^{13}\,\mathcal{M}_\odot$ and $\mathcal{M}/\mathcal{L}_R \sim 3000$), in other words, a "dark lens".

The availability of large telescopes allows to push further the direct search for a putative lens in the vicinity of the two quasar components. Alternatively, if there were a massive dark lens in the field of LBQS 1429-0053 it would produce a weak but measurable distortion on all background galaxies. Looking for a weak lensing effect is another way of revealing a dark lens, using wide-field deep observations. This method has been used and has led to positive detections on wide field images of Q2345+007 (Bonnet et al. 1993) and MG 2016+112 (Benitez et al. 1999). The cluster responsible for the weak lensing signal in MG 2016+112 has recently been confirmed spectroscopically (Soucail et al. 2001).

We have observed LBQS 1429-0053 in the course of a larger project aimed at analyzing in detail the mass distribution towards a large number of known multiply-imaged quasars and towards some suspected lenses. The ESO 8.2 m VLT allowed to reach limiting magnitudes of $R = 27.0$, $J = 24.0$ and $Ks = 22.5$ ($3\sigma$), in conditions of very good image quality, for most of our targets.

In Sect. 2, we discuss the VLT and HST observations and the data reduction. In Sect. 3 we present the photometric properties of the quasar pair LBQS 1429-0053 A and B and of the closest galaxies, as inferred either from PSF subtracted or deconvolved images in the *R*-, *J*-, *H*- and *Ks*-bands. We discuss in Sect. 4 the galaxies close to the quasar components and the possible detection of the quasar host galaxy. Two different methods to look for the putative lensing potential are discussed in Sect. 5. Finally, two tentative lens models are discussed, while the results and conclusions of the paper are summarized in Sect. 6. We adopt $H_0 = 65$ km s$^{-1}$ Mpc$^{-1}$, $\Omega = 0.3$ and $\Lambda = 0.7$ throughout.

**Table 1.** Summary of the instrumental configuration used for the optical and near-IR observations of LBQS 1429-0053. The columns display respectively the date of observation, the telescope and instrument used, the filter, the image quality ($IQ$), and the total exposure time in kilo-seconds.

| Date | Instrument | Filter | $IQ$ | Time |
|---|---|---|---|---|
| 2001 Jun. 08,15 | VLT-ISAAC | $Ks$ | 0.64″ | 3.7 |
| 2001 Jun. 08 | VLT-ISAAC | $J$ | 0.50″ | 2.6 |
| 2001 Apr. 18 | VLT-FORS1 | $R$ | 0.55″ | 3.6 |
| 1997 Dec. 30 | HST-NICMOS | $H$ | 0.16″ | 2.6 |

## 2. Observations and data reduction

The ground-based observations presented in this paper were taken with the Infrared Spectrometer And Array Camera (ISAAC, Cuby et al. 2002) and the Focal Reducer/low dispersion Spectrograph (FORS1, Szeifert 2002) attached to the 8.2 m telescope VLT/ANTU, at ESO/Paranal. The observations were obtained in Period 67 as part of programs 67.A-502(A, B, C). Observations with the Hubble Space Telescope (HST) and the near-IR NICMOS instrument were all retrieved from the HST/STScI archive. Detailed information about the observational setup and conditions are presented hereafter.

### 2.1. VLT observations

Direct near-IR ISAAC imaging in the *J*- and *Ks*-bands has been carried out with the Short Wavelength Imaging camera (SWI1) equipped with a Rockwell-Hawaii (RH) $1024 \times 1024$ pixel array. The scale is 0.1484″ per pixel and the field-of-view, $2.5' \times 2.5'$. The scientific and calibration frames were corrected for the odd-even column effect arising from an ISAAC misfunction during the nights of observation: this artifact was successfully removed through a Fourier analysis procedure (see ISAAC handbook, Cuby et al. 2002). Standard reduction procedures were then applied to subtract the dark and to flat-field the images using a normalized flat. Sky subtraction and co-addition of the reduced dithered frames were performed using tasks from XDIM/IRAF.

The FORS1 instrument was used to carry out the *R*-band observations using the standard resolution collimator (SR). The resulting scale is 0.2″ per pixel and the useful field-of-view is $6.8' \times 6.8'$. The *R*-band data were reduced using sky flat-fields and standard IRAF routines. A summary of the main observational parameters can be found in Table 1.

### 2.2. Hubble space telescope observations

HST archival data of LBQS 1429-0053 are available as part of a much larger public survey of gravitational lenses (PI: E. Falco) known as the CfA-Arizona Space Telescope LEns Survey (CASTLES, Kochanek et al. 2002). The NICMOS2/F160W

($H$-band) data were taken on 1997 December 12, with a total exposure time of $4 \times 640$ s. At the date of observation the NICMOS2 pixel size was $0.0760'' \times 0.0753''$. We constructed a mosaic of the flux calibrated frames using standard IRAF procedures. The final image is a simple combination of the frames. In performing the image combination, a mask image has been created and used to remove bad pixels and cosmic rays. The resolution of the combined image is $\sim 0.16''$ ($FWHM$).

## 3. Subtraction of the quasar components and deconvolution

In the first place, combined images are used to search for the presence of a single lens very close to the quasar components. Even under excellent seeing one should apply numerical techniques to extract the signal in an optimum way. We used three techniques: subtraction of the telescope Point-Spread-Function (PSF) and two different image deconvolution techniques in order to validate the detection of any faint source.

### 3.1. PSF-subtraction

The determination of the PSF was performed using DAOPHOT (Stetson 1987). This software decomposes the PSF into the sum of an analytical profile (a Moffat profile in the present case) and a residual map. The analytical profile and the residual map are computed from as many stars as possible across the frame in order to optimize the signal-to-noise ratio of the PSF. In the case of the ISAAC observations, the task is complicated by a slight non-linearity of the ISAAC detector (1% at 10 000 ADU). This non-linearity may affect the two quasar components in a different way, as their magnitude difference is large, $\Delta J \sim \Delta K \sim 3.6$. Two PSFs were therefore constructed, using stars with a brightness comparable to that of the object to be subtracted: a "faint PSF" was built for quasar B (from 2 stars), while a "bright PSF" was built for quasar A (from 5 stars).

The $R$-band image is not affected by non-linearity effects. However, the center of LBQS 1429-0053 A is saturated. We setup a special core-correction for the PSF subtraction, giving more weight to the wings of the PSF than to its core: this is limiting the area over which one can trust the PSF subtraction but allows accurate subtraction of the PSF wings.

The PSF determination for the HST/NICMOS2 data was performed in a different way. The small field-of-view and the absence of stellar objects close to the quasar components make it impossible to construct an empirical PSF. Instead, we have used the TinyTim V6.0 software (Krist & Hook 2001) to model the NICMOS2/F160W PSF over $3'' \times 3''$. We have assumed a flat spectrum for the quasars across the F160W filter. The PSF has been oversampled with $5 \times 5$ sub-pixels in order to improve the accuracy of the centering of the PSF before the subtraction is carried out. PSFs were computed at the position of the two quasar components, were fitted independently and subtracted from the quasar images.

### 3.2. Image deconvolution

Two algorithms were used for image deconvolution: the Maximum Entropy Method (MEM; Cornwell & Evans 1985) and the MCS deconvolution algorithm (Magain et al. 1998).

In the case of the MEM procedure, we have deconvolved fields of $13'' \times 13''$ ($R$-, $J$- and $Ks$-bands), around the quasar components. We have used the PSFs constructed for PSF subtraction and described above.

The PSF used for the MCS deconvolution is similar to that described in Sect. 3.1, but without taking into account the non-linearity of ISAAC. This does not affect seriously the $J$-band observations although it introduces extra residuals close to quasar A in the $Ks$ filter. Since quasar A is saturated in the $R$-band, 5 central pixels of its image were not used in the deconvolution. The MCS deconvolution algorithm allows to choose the final image pixel size. We have adopted for each band a pixel size two times smaller than in the original data. The resolution after processing is $FWHM_R = 0.30''$, $FWHM_J = 0.21''$ and $FWHM_{Ks} = 0.21''$. The MCS deconvolution algorithm produces deconvolved images and residual maps which allow to check locally whether the deconvolved image is compatible with the data (see Courbin et al. 1998 for more details). Close to quasar A, the residuals remain significant. The size of the area with significant residuals can be taken as the size of the zone where it is not possible to detect a faint structure. This zone has a radius of $0.3''$ in $R$ and $J$, and a radius of $0.6''$ in $Ks$, more affected by the non-linearity of the detector. We performed the astrometry and photometry of LBQS 1429-0053 A and B, as well as of the objects identified on the deconvolved images. Results are given in Table 2.

### 3.3. Results of the PSF subtraction and of deconvolution

Results of the PSF subtraction are displayed in Figs. 1 to 4. We estimate that sources could not be detected if they were located within radii of $1.0''$ ($R$), $0.5''$ ($J$), $0.7''$ ($H$) and $0.6''$ ($Ks$) from component A, because of the difficulty to build a PSF as bright as quasar A. On the contrary, for quasar B, faint sources could be detected after PSF subtraction, without spatial limitation. Some residual signal above the sky background can be detected after the PSF subtraction of components A and B, at the level of $1.8\sigma$ in $Ks$ and $2.0\sigma$ in $J$. It is unclear whether these extended residuals are artifacts of the PSF subtraction or real faint extended sources.

In order to set the limits of this detection, we have added a fake elliptical galaxy of a size comparable to that of galaxy #1 found in the environment of the quasars (major axis $a = 0.8''$, minor axis $b = 0.4''$). This simulation has been made on the $R$, $J$ and $Ks$ images, placing the fake at various positions across the image: (a) $0.8''$ East to the center of quasar A, (b) $0.4''$ West to the center of quasar B (these positions are within the wings of the quasar images), (c) $7''$ South-West to the center of quasar A, where no signal had been detected after PSF subtraction or deconvolution. These simulated frames have been deconvolved using the MEM procedure, in a way similar to that described in Sect. 3.2. We increased the magnitude of the

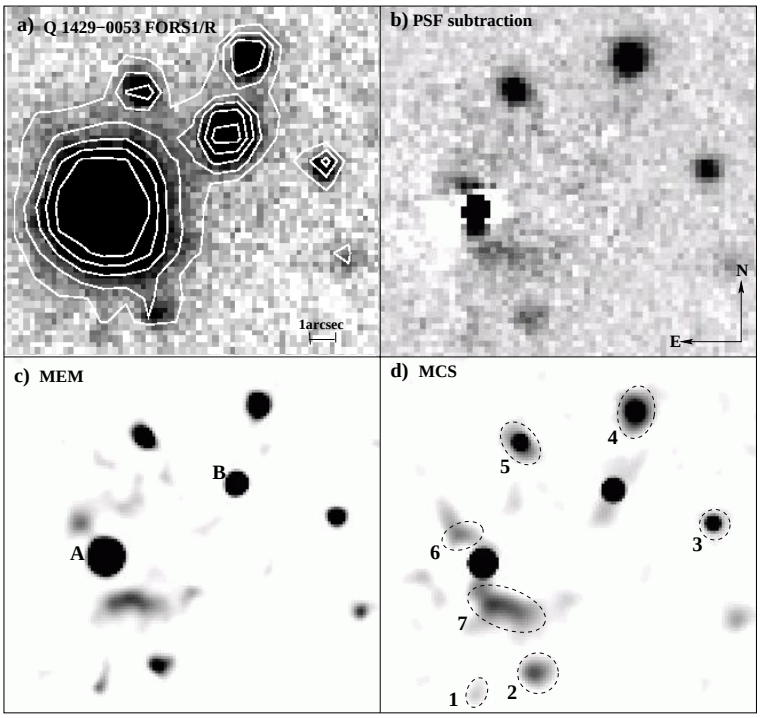


**Fig. 1. a)** The 13″ × 13″ *R*-band field around LBQS 1429-0053 A and B from FORS1. North is to the top, East is to the left. **b)** Same area, but with the PSF subtracted on components A and B as explained in Sect. 3.1. **c)** Result of the MEM deconvolution (Sect. 3.2): A and B are the two quasar components. **d)** Result of the MCS deconvolution (Sect. 3.2). The photometric properties of the faint objects labeled #1 to 7 are described in Sect. 4 and Table 2.

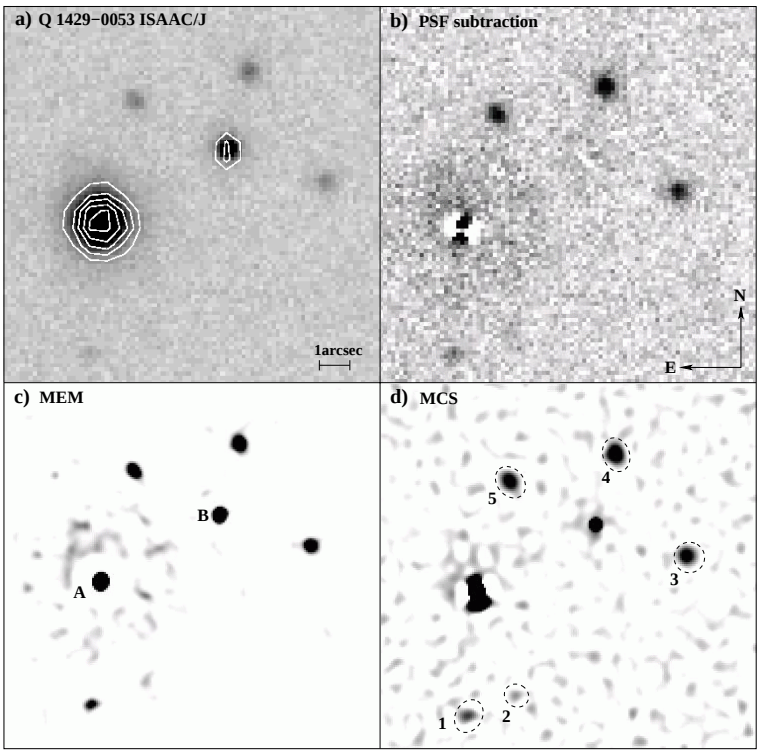


**Fig. 2. a)** The 13″×13″ *J*-band field around LBQS 1429-0053 from ISAAC. North is to the top, East is to the left. **b)** Same area, but with the PSF subtracted on components A and B (Sect. 3.1). **c)** Result of the MEM deconvolution (Sect. 3.2): A and B are the two quasar components. **d)** Result of the MCS deconvolution (Sect. 3.2). The photometric properties of the faint objects labeled #1 to 5 are described in Sect. 4 and Table 2.

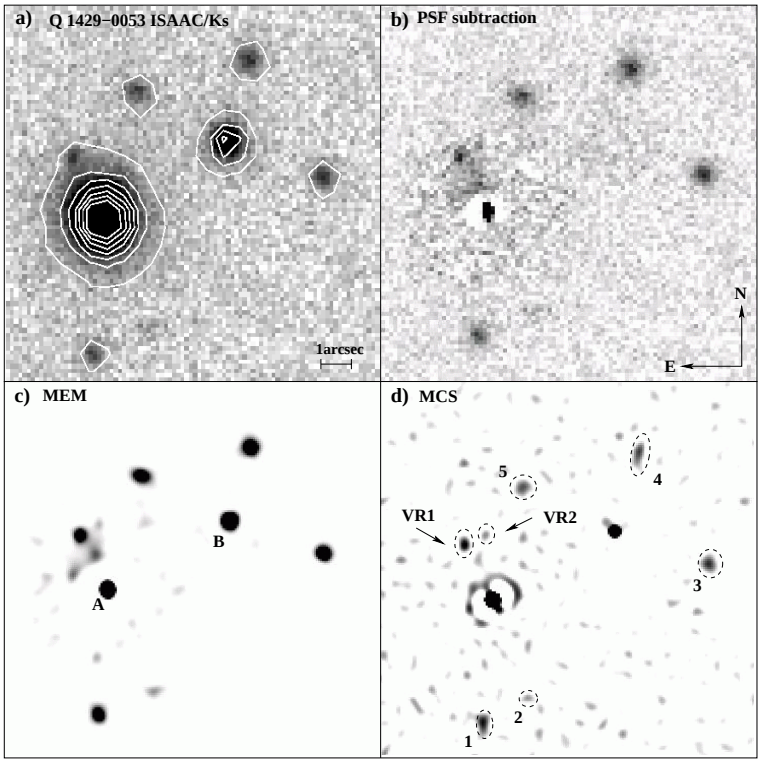


**Fig. 3. a)** The 13″×13″$Ks$-band field around LBQS 1429-0053 from ISAAC. North is to the top, East is to the left. **b)** Same area, but with the PSF subtracted on components A and B (see Sect. 3.1 for details). **c)** Result of the MEM deconvolution (Sect. 3.2): A and B are the two quasar components. **d)** Result of the MCS deconvolution (Sect. 3.2). Two very red objects, VR1 and VR2 are identified to the North of component A in addition to the objects #1 to 5 (Sect. 4 and Table 2).

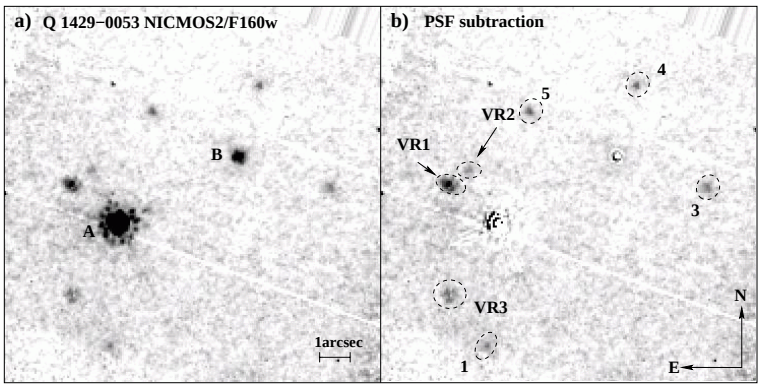


**Fig. 4. a)** The 13″×13″$H$-band field around LBQS 1429-0053 from HST/NICMOS2. A and B are the two quasar components. North is to the top, East is to the left. **b)** Same area, but with the PSF subtracted on components A and B (Sect. 3.1 for details). The faint objects identified in the field are objects previously identified as #1, 3, 4 and 5 , as well as three very red objects: VR1 and VR2 to the North of quasar A, and VR3, to the South (Sect. 4 and Table 2).

fake by steps of 0.5 from $R = 24$, $J = 21$ and $Ks = 20$ up to the magnitudes at which a galaxy could not be detected above the noise ($S/N = 1$). These limiting magnitudes are displayed in Table 3. Comparing to the apparent magnitude of an elliptical galaxy with $M^{\star}_{B_T} = -20.59$ (Cheng & Krauss 2001) at different redshifts, this simulation allows to infer the maximum redshift accessible in our processed dataset, as a function of the putative lens position. In the case of a lensing galaxy located between the two quasars (position c), or very close to quasar B (position b), we would easily probe until the quasar redshift ($z_{\rm quasar} = 2.076$) after deconvolution. We conclude that no galaxy with $\mathcal{L} \sim \mathcal{L}^{\star}$ is detected in this area. If the putative lens were located on the wings of quasar A (position a), we could detect it up to $z = 1.9$ (see Table 3) . Such a source would be too close to the quasar itself to act as a lensing object.

## 4. The quasars and their immediate vicinity

The magnitude differences between the two quasars in the four bands are displayed in Table 2. They vary between 3.4 and 3.7 mag, depending on the band. In the case of gravitational lensing, this value should in principle be constant, whatever the

**Table 2.** Photometry of the objects in the 13″×13″ deconvolved field. The IDs correspond to sources identified in Figs. 1, 2, 3 and 4. The columns successively provide: (1) the object identification, (2–3) the coordinates relative to A, (4–7) the *R*, *J*, *H* and *Ks* magnitudes, (8–9) the redshift (spectroscopic redshift for A and B, photometric redshift for other objects) and the corresponding error bars, (10) some comments or references. The second line provides the date of observation, while the fifth line provides the magnitude differences between quasars A and B.

| ID | $\Delta\alpha$ (″) | $\Delta\delta$ (″) | *R* Apr. 2001 | *J* Jun. 2001 | $H_{\rm F160w}$ Dec. 1997 | *Ks* Jun. 2001 | *z* | $\Delta z$ | Comments |
|---|---|---|---|---|---|---|---|---|---|
| A | 0 | 0 | 17.45 ± 0.02 | 16.32 ± 0.01 | 15.88 ± 0.01 | 14.96 ± 0.01 | 2.076 | 0.02 | Hewett et al. |
| B | −4.455 ± 0.005 | +2.489 ± 0.005 | 20.85 ± 0.02 | 20.00 ± 0.01 | 19.27 ± 0.01 | 18.58 ± 0.01 | 2.076 | 0.02 | (1989) |
| $\Delta\, m_{\rm AB}$ | | | 3.40 ± 0.02 | 3.68 ± 0.01 | 3.39 ± 0.01 | 3.62 ± 0.01 | | | |
| 1 | +0.3 ± 0.051 | −4.50 ± 0.10 | 26.08 ± 0.05 | 22.66 ± 0.15 | 22.18 ± 0.05 | 20.08 ± 0.17 | 1.1 | 1.0–1.3 | $\chi^2 > 1$ |
| 2 | −1.50 ± 0.20 | −3.70 ± 0.20 | 24.43 ± 0.05 | 23.81 ± 0.20 | >22.5 | 21.35 ± 0.30 | – | – | – |
| 3 | −7.86 ± 0.01 | −1.33 ± 0.02 | 24.52 ± 0.02 | 21.69 ± 0.08 | 20.92 ± 0.03 | 20.02 ± 0.15 | 0.8 | 0.6–1.1 | – |
| 4 | −5.23 ± 0.04 | +5.23 ± 0.08 | 22.71 ± 0.04 | 21.34 ± 0.06 | 21.52 ± 0.05 | 20.16 ± 0.20 | 1.3 | 1.0–1.9 | $\chi^2$ >1 |
| 5 | −1.22 ± 0.14 | +4.11 ± 0.02 | 23.53 ± 0.06 | 21.66 ± 0.07 | 21.17 ± 0.04 | 20.30 ± 0.15 | 1.2 | 0.8–1.9 | – |
| 6 | +0.82 ± 0.10 | +0.96 ± 0.10 | 24.89 ± 0.06 | >24.5 | >22.5 | >24.5 | – | – | – |
| 7 | −0.55 ± 0.10 | +1.43 ± 0.10 | 23.18 ± 0.02 | >24.5 | >22.5 | >24.5 | – | – | – |
| VR1 | +1.02 ± 0.10 | +2.01 ± 0.10 | >27 | >24.5 | 19.30 ± 0.01 | 20.49 ± 0.15 | – | – | – |
| VR2 | +0.26 ± 0.10 | +2.36 ± 0.10 | >27 | >24.5 | 21.69 ± 0.04 | 21.60 ± 0.40 | – | – | – |
| VR3 | +1.60 ± 0.10 | −2.6 ± 0.10 | >27 | >24.5 | 20.99 ± 0.03 | >24.5 | – | – | – |

**Table 3.** Lower limit magnitude of detectability of a putative lensing galaxy according to its position (Cols. 2, 3 and 4). Column 5 displays the minimal redshift for an $\mathcal{L}^*$ galaxy of this magnitude.

| Position | *R* | *J* | *Ks* | |
|---|---|---|---|---|
| (a) 0.8″ East to A | 25.5 | 24.0 | 22.5 | $z > 1.9$ |
| (b) 0.4″ West to B | 26.5 | 24.5 | 24.5 | $z > 3.2$ |
| (c) 7.0″ South-West to A | 27.0 | 24.5 | 24.5 | $z > 4.5$ |

wavelength is. However, such small variations may arise from various effects. For example, the intrinsic temporal variability of the quasars could explain the lowest $\Delta m_{AB}$ in the *H*-band, taken 4 years before the *J* and *Ks* datasets (similar case for the quasar SBS 1520+530 studied by Faure et al. 2002). Also, the *R*-band image is expected to be more affected by absorption than the near-IR images. As the quasars are separated by 5.1″, the different $\Delta m_{AB}$ measured could probe the presence of different absorbers along the line of sight towards the quasars A and B. Finally, microlensing effects could also explain these small differences (<0.3 mag) between the different bands. In conclusion, the variation with wavelength of the intensity ratio between the two quasars does not allow to reject the hypothesis of a lens for this system.

Objects #1, 3, 4 and 5 being detected in the 4 bands, we can tentatively estimate their photometric redshifts. We use the Hyperz software, a SED fitting procedure based on the fit of the overall shape of the galaxy spectra and on the detection of prominent spectral features (Bolzonella et al. 2000). The observed photometric SED is compared to those obtained from a set of reference spectra (spectral evolution library of Bruzual & Charlot 1993), using the same photometric system. The observed galaxy flux is corrected for reddening following the Calzetti law (Calzetti et al. 2000). Hyperz performs a $\chi^2$ minimization and the redshift given in Table 2 corresponds to the lowest $\chi^2$ (ideally $\chi^2$ <1), while the photometric redshift error bars are the extrema of the confidence interval at 68%. Our set of filters allows to bracket the 4000 Å break from $z \geq 0.5$. Yet, it has been shown that 4 bands is still too few to derive accurate photometric redshifts (Bolzonella et al. 2000; Athreya et al. 2002). With this remark in mind, we find a mean redshift of $z \sim 1$ for objects #1, 3, 4 and 5 (with error bars up to 50%), the SED of objects #1, 3 and 5 being best fitted by a starburst type galaxy, and that of object #5, by an Im type galaxy. Object #2, which is not detected in the *H*-band, shows magnitudes in the other bands comparable to those of galaxies #1, 3, 4 and 5.

Two objects, close to quasar A, are detected only in the *R*-band. They are labeled #6 and 7 in Table 2 and may be in fact one single object, artificially separated by the deconvolution and PSF subtraction procedures at the position of quasar A. These objects could pertain to the image of the amplified and distorted quasar host galaxy. In this case, we would expect a counter-image of object #6 in the B component of the quasar, to have $R \sim 28.3$, according to the flux ratio measured between quasars A and B. The counter-image of object #7 would be expected at $R \sim 26.6$. This is at the limit of the data, and although some very faint, non significant residuals are seen close to image B (see Fig. 1) we cannot report on any firm detection of the quasar host counter-image in component B. Given our detection limits in the near-IR, and given the colors of a typical quasar host, we do not expect to see any trace of a near-IR counterpart of objects #6 and #7 in our ISAAC observations. Our observation in the *R*-band is therefore consistent with the detection of the quasar host, but it could well be also a relatively blue object at low redshift.

Finally, 3 very red objects (VR1, VR2 and VR3 in Fig. 4) only visible in the *H*- and *Ks*-bands, are seen close to quasar A. VR1 and VR2 have $R-K > 5.3$ and thus are belonging to the ERO class of objects (e.g. Thompson et al. 1999). VR2 is at the detection limit of the VLT data, and its

position for flux measurement was inferred from the HST data.VR3 is only detected in $H$ with $R-H > 6$. If these objects are at the redshift of the quasar, the 4000 Å break falls between the $J$- and $H$-bands and would explain the observed red colors. Alternatively, they could be obscured star forming galaxies at redshift ∼1 (e.g. Spinrad et al. 1997; Cohen et al. 1999; Smith et al. 2002a and 2002b). In that case, they might have redshifts compatible with those of objects #1, 3, 4 and 5 and be faint members of a galaxy group at $z \sim 1$.

## 5. Looking for a cluster lens

The spatial distribution of objects in the field of LBQS 1429-0053 has been investigated. Object catalogs have been constructed in the $R$-, $J$-, $H$- and $Ks$-bands, using the SExtractor 1.2 software (Bertin & Arnouts 1996). The separation between stars and galaxies was made using a combination of the $FWHM$ versus magnitude plot and of the analysis of the peak surface brightness $\mu_{\max}$ (mag arcsec$^{-2}$) of the objects versus their total magnitude (Bardeau et al. 2003). As a matter of fact, non-saturated stars are bright point-like objects of the size of the PSF. Therefore, in the $FWHM$ versus magnitude plot, they are easily detectable on an horizontal line. Moreover, the stars have the highest peak surface brightness, and for stars, $\mu_{\max}$ increases linearly with magnitude. Therefore, using these two plots it is possible to separate galaxies from stars in our catalogs of objects. Finally, our photometric catalogs are composed of ∼3000 galaxies in $R$, and ∼250 in $J$ and $Ks$.

### 5.1. Isodensity contours

We have used the $6.8' \times 6.8'$ $R$-band image to compute the isodensity contours of the galaxy distribution. The galaxy catalog has been split in three magnitude bins ($22 \leq R < 24$, $23 \leq R < 25$, $24 \leq R < 27$) that allow to study roughly 3 redshift slices. As we do not have any reference-field of the same depth for comparison, we have determined the mean background galaxy density from the data itself, dividing the image into a grid of $20 \times 20$ contiguous cells of $20''$ side. The cell size corresponds to 50 kpc at $z = 1$. The galaxy density is measured in each cell and an histogram is constructed of the frequency of occurrence of each density (right panel of Fig. 5 for the magnitude range $23 \leq R < 25$). A Gaussian is fitted to the histogram, giving a mean density and a standard deviation which will be used in estimating the significance of an eventual cluster detection. A $2.5\sigma$ deviation (20.2 galaxy per arcmin$^2$ in this plot) away from the mean can be considered as a significant galaxy overdensity.

The distribution of bright galaxies ($22 \leq R < 24$) does not show any significant overdensity. Taking into account all very faint objects down to our limiting magnitude ($24 \leq R < 27$) does not allow either to unveil any overdensity. Cutting the faint end of our galaxy catalog ($23 \leq R < 25$), i.e., removing possible spurious detections, results in one peak located 2.3′ South-East to LBQS 1429-0053A. (left panel of Fig. 5). This overdensity is too far away from the quasars to be the source of any lensing effect. We have performed a similar analysis for the $J$ and $Ks$ images, and do not find any galaxy overdensity above $2.5\sigma$.

### 5.2. Weak-shear analysis

If LBQS 1429-0053 is lensed by a group of galaxies or a cluster of galaxies (dark or visible), a weak lensing analysis of the field should reveal it. The best available data to carry out this experiment is the $R$-band image, which is very deep (limiting magnitude in $R = 27$ mag) and has the largest field-of-view ($6.8' \times 6.8'$).

The statistical distortions of field galaxies by a galaxy cluster, can be quantified by measuring the mean ellipticity of many faint galaxies in cells of a given size. This size has to be chosen carefully: if it is much larger than the scale of an appreciable variation of the potential, the averaging will destroy the coherence of the distortion pattern, while if the cells are too small, the averaging will not remove the effect of galaxy intrinsic ellipticities from the distortion estimation and the result will be dominated by shot-noise.

For any weak-lensing signal to be accurately measured, the first step is to correct the observed galaxy ellipticities for the instrumental distortions. To do this, the PSF variation is measured across the field from 175 stars, using the *Im2shape* software (Bridle et al. 2002). The ellipticity of the PSF varies from $\epsilon = (a-b)/(a+b) = 0.009$ to 0.034 across the FORS1 field. Each background galaxy ($R \geq 23$ mag) is deconvolved in an analytical way, modeling it by an adequate 2D-function and using the closest PSF. The corrected galaxy ellipticities are averaged in cells of $20'' \times 20''$ size, which allow to use 10 to 50 galaxies by cell. The mean ellipticity of the galaxies vary from $\epsilon = (a-b)/(a+b) = 0.05$ to 0.23 across the image. In a field revealing weak shear, we expect the mean ellipticities from one cell to the other to be correlated. In Fig. 6 (top panel) we display the shear-map, where each stick orientation shows the mean galaxy orientation in the cell, and where the length of the stick is proportional to the mean ellipticity $\epsilon$. The mean ellipticity over the FORS field computed as $(< e_1 >, < e_2 >)$[1] is $(-0.04 +/- 0.03, 0.00 +/- 0.04)$. It does indicate a slight preferred orientation along the horizontal axis, but this is consistent with the typical cosmic variance. Thus, there is no evidence that a strong lens is present in the vicinity of this field. The weak shear analysis of the $J$ and $Ks$ frames reveals features similar to those in the $R$-band, and therefore does not show either any coherent distribution of the mean galaxy ellipticities revealing the presence of a galaxy cluster in our field-of-view.

We used the maximum-entropy algorithm *LensENT2* (Bridle et al. 1998; Marshall et al. 2002) to study the spatial distribution of the mass. The lens plane is assumed to be at $z = 1$ (corresponding to the mean redshift of the closest faint galaxies detected near quasar A, see Sect. 4). The weak shear has been computed for galaxies with $R \geq 23$. The mass profile or Intrinsic Correlation Function (ICF) of the mass clumps is assumed to be Gaussian. The width of the ICF, that defines the final spatial resolution of the map, is not intrinsically

[1] $< e_1 > = < \epsilon_i \times \cos(2 \times \theta_i) >$ and $< e_2 > = < \epsilon_i \times \sin(2 \times \theta_i) >$, for each stick $i$.

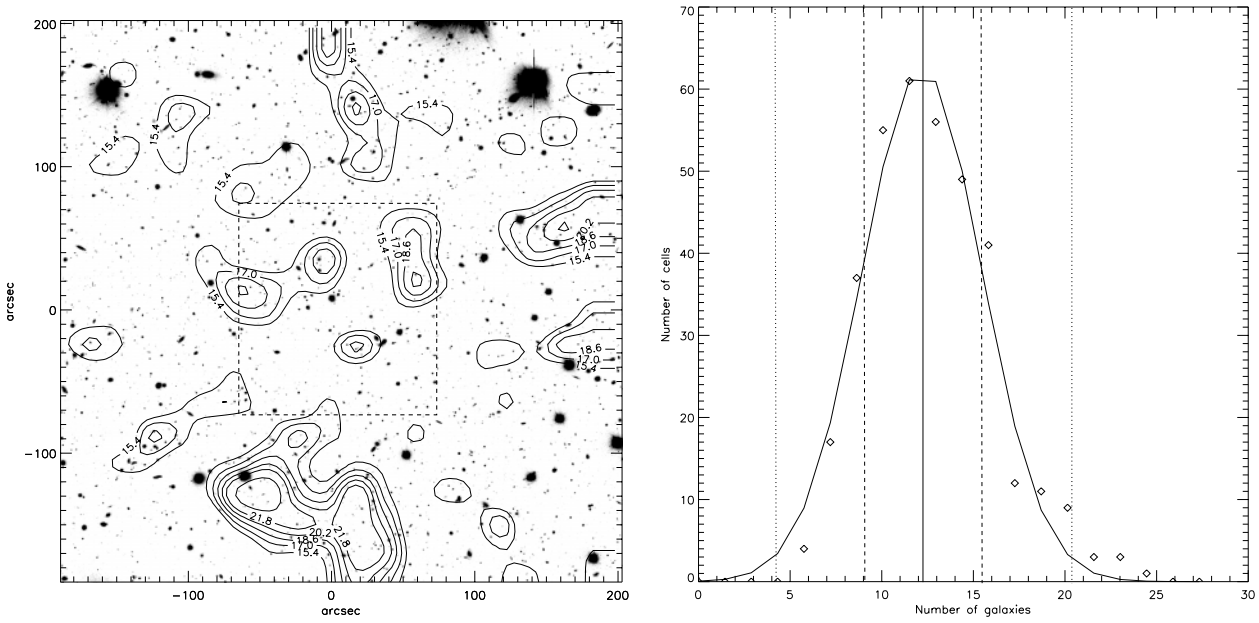


**Fig. 5.** The left panel displays the number density isocontours for the magnitude range $23 \leq R < 25$, superimposed on the FORS1 image. The coordinate (0,0) indicates the location of LBQS 1429-0053 A. The contours outline the regions of constant density. Labels of the contours display the number of galaxies per arcmin$^2$ (starting at $1\sigma$, and then, $1.5\sigma$, $2\sigma$, $2.5\sigma$, $3\sigma$ and $4\sigma$). The dashed square represents the ISAAC field-of-view. North is to the top, East to the left. The right panel shows the number of cells in the field which have a given galaxy density (galaxies per arcmin$^2$). The Gaussian fits the points corresponding to cells which are assumed to be filled with background galaxies. The solid vertical line displays the mean galaxy density of the distribution, whereas the dashed and dotted lines are respectively at $1\sigma$ and $2.5\sigma$.

constrained due to the low coherence in the shear pattern. An ICF of 60″ was therefore assumed. The reconstructed mass map is shown in Fig. 6 (bottom panel).

Since the noise properties of maximum-entropy inversion methods are not easily interpretable, we have performed 100 reconstructions on modified catalogs of galaxies for which positions are retained but ellipticity directions are assigned at random. We have compared the level of the structures detected in the reconstructed map to the bootstrap sample: the highest peak (2.8′, North-East to LBQS 1429-0053 A) in the map reconstructed from our dataset is 1.2 times higher than the highest peak in the bootstrap sample. Thus, our detection is very close to the noise level.

If it were actually a signal, let us quantify it in term of mass. We performed the following simulation: assuming that the field galaxies above $R = 23$ mag are background galaxies with a mean redshift of $z = 1.5$, we have added a Spherical Isothermal Sphere (SIS) at $z = 1$ in the line of sight towards this field, and we have computed its influence on the background galaxies. The resulting fake frame has been analyzed in a way similar to the original frame: we performed a weak-shear analysis and a mass reconstruction. To discard the risk of having superimposed the SIS on top of a possible faint and undetected mass potential, we did the simulation for several SIS positions across the field-of-view: 2′ South-East, 2′ South-West, 2′ North-West and 2′ North-East to LBQS 1429-0053 A, as well as at the position of LBQS 1429-0053 A. We have varied the mass of the potential until we could detect clumps in the reconstructed mass map of the same level as in the original data. This mass varies between $1.2\times10^{13}\,\mathcal{M}_\odot$ arcmin$^{-1}$ and $2.5\times10^{13}\,\mathcal{M}_\odot$ arcmin$^{-1}$ (from 3 to $6\times10^{13}\,\mathcal{M}_\odot$ for a lens at $z = 1$), or, in terms of velocity dispersion, between $\sigma_v = 320$ and 500 km s$^{-1}$. This is the limit to the detection of weak lensing in this field using the current data.

## 6. Conclusions

Using deep VLT and HST images, we have searched, on several scales, for a gravitational lens in the field of the quasar pair LBQS 1429-0053 A and B.

On the scale of galaxy cluster, we do not detect any significant galaxy overdensity in a $6.8' \times 6.8'$ field around the quasar pair, down to $R \sim 27$. Under the hypothesis of a dark lens, we have performed a weak lensing analysis. Although our technique would allow to detect mass concentrations down to $1.2$–$2.5\times10^{13}\,\mathcal{M}_\odot$ arcmin$^{-1}$, we do not detect any coherent shear pattern on faint field galaxies. We conclude that there is no evidence for a large scale lens in the field of LBQS 1429-0053, whether it be luminous or dark.

On smaller scales (∼1–5″), no luminous object is detected between the quasar images down to our limiting magnitudes in the four filters (27 mag in $R$, 24 mag in $J$ and 22.5 mag in $Ks$) . If the lens in LBQS 1429-0053 were within the usual redshift range observed for lens galaxies ($0 < z < 1$), simple (and vastly under constrained) modeling with an isothermal sphere shows that the velocity dispersion of the lens should be of the order of 350 km s$^{-1}$. According to the Faber-Jackson relation, this implies a galaxy 6 times brighter than an $\mathcal{L}_\star$ galaxy ($\mathcal{M}/\mathcal{L}_J \sim 3000$), which would be easily detected given the depth of the available dataset. Tentative modeling of a multiple

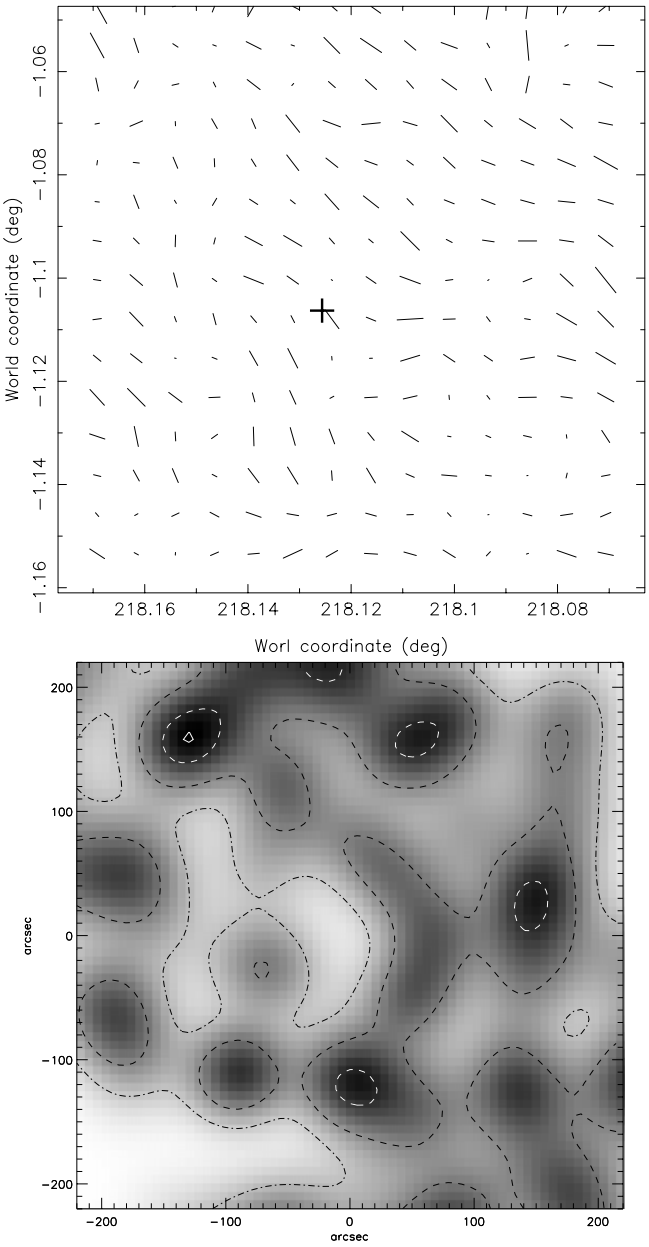


**Fig. 6.** The top panel shows the shear map for the 6.8′ ×6.8′ field-of-view around the quasars. Each stick displays the mean direction of galaxies in a cell of 30″×30″ ($\epsilon_{\max} = 0.23$). The coordinates (218.125, −1.105) indicates the position of LBQS 1429-0053 A (black cross). The bottom panel shows the surface mass density from the maximum-entropy mass reconstruction. On this grey-scale,white corresponds to the lowest mass level, and black corresponds to the highest mass level. The contours successively outline regions of signal to noise: 0.3 (black dotted-dashed line), 0.6 (black dashed line), 1 (white dashed line) and 1.2 (white continuous line), the noise level being computed from the bootstrap sample.

lens has been carried out, involving objects #1 to 5 in the immediate vicinity of the quasar pair. These objects have similar colors, compatible with ellipticals at $z \sim 1$. We failed however in reproducing both the image separation and flux ratios, using such a model. The group of 5 galaxies cannot be alone responsible for the LBQS 1429-0053 A and B configuration, would it be a lensed quasar.

Finally, the only remaining sign of lensing is the detection of what might be the lensed host galaxy of LBQS 1429-0053, detected in the *R*-band, as objects #6 and 7. Given the limiting magnitudes in the other filters, we do not expect to detect it in the near-IR, nor do we expect to see its counter-image in the B component of LBQS 1429-0053. Another possibility is that this object is a foreground blue object, unrelated to the quasar. Two observations might settle the issue. First, a deep HST image with $R > 27$, as could be obtained with the Advanced Camera for Surveys should allow to constrain the morphology of objects #6 and 7 well enough, both for quasar A and their counter-part for quasar B, to decide whether it is the quasar host galaxy stretched by lensing or whether it is a foreground object. Second, the photometric monitoring and the measurement of a time delay would establish the lensed nature of LBQS 1429-0053. The first observation is straightforward and would settle the issue straight. The second observation is more telescope time consuming.

With the present observational material, we conclude that there is very little evidence that LBQS 1429-0053 is lensed, either by a galaxy cluster, or a galaxy group or a single galaxy (dark or luminous) and thus, should be considered as a genuine binary quasar.

*Acknowledgements.* We acknowledge the guidance of Andreas Jaunsen in the NICMOS2 data reduction. Micol Bolzonella provided help in the application of the Hyperz software to the present dataset. We are indebted to an anonymous referee for interesting comments. The HST data used in this paper were obtained by the "CfA Arizona Space Telescope LEns Survey" (CASTLES) collaboration (PI: E. Falco). Cécile Faure acknowledges support from an ESO studentship in Santiago. Frédéric Courbin is supported by Marie Curie grant MCFI-2001-00242. The collaborative grant ECOS/CONICYT CU00U005 between Chile and France is also gratefully acknowledged. Jean-Paul Kneib thanks CNRS for support as well as the ESO Chile visitor program.

## References

Athreya, R., Mellier, Y., van Waerbeke, L., et al. 2002, A&A, 384, 743
Bardeau, S., Kneib, J.-P., Czoske, O., et al. 2003, in preparation
Benitez, N., Broadhurst, T., Rosati, P., et al. 1999, ApJ, 527, 31
Bertin, E., & Arnouts, S. 1996, A&AS, 117, 393
Bonnet, H., Fort, B., Kneib, J.-P., et al. 1993, A&A, 280, L7
Bolzonella, M., Miralles, J.-M., & Pelló, R. 2000, A&A, 363, 476
Bridle, S., Hobson, M., Lasenby, A., et al. 1998, MNRAS, 299, 895
Bridle, S., et al. 2002, in preparation
Bruzual, A., & Charlot, S. 1993, ApJ, 405, 538
Calzetti, D., Armus, L., Bohlin, R. C., et al. 2000, ApJ, 533, 682
Cheng, Y.-C., & Krauss, L. M. 2001, NewA, 6, 249
Cohen, J. G., Hogg, D. W., Pahre, M. A., et al. 1999, ApJ, 120, 171
Cornwell, T. J., & Evans, K. F. 1985, A&A, 143, 77
Courbin, F., Lidman, C., & Magain, P. 1998, A&A, 330, 57
Cuby, J. G., Lidman, C., Moutou, C., et al. 2002, ISAAC handbook
Faure, C., Courbin, F., Kneib, J. P., et al. 2002, A&A, 386, 69
Hewett, P., Webster, R., Harding, M., et al. 1989, ApJ, 346, L61
Hjorth, J., & Kneib, J.-P. 2002, submitted to ApJ
Kneib, J.-P., Mellier, Y., Fort, B., et al. 1993, A&A, 273, 367
Kneib, J.-P., Alloin, D., & Pelló, R. 1998, A&A, 339, L65

Kochanek, C. S., Falco, E. E., & Muñoz, J. A. 1999, ApJ, 510, 590
Kochanek, C. S., Falco E. E., Impey, C., et al. 2002, *The CASTLE Survey*: http://cfa-www.harvard.edu/glensdata/
Krist, J., & Hook, R. 2002, *The Tiny Tim User's Guide*: http://www.stsci.edu/software/tinytim
Magain, P., Courbin, F., & Sohy, S. 1998, ApJ, 494, 472
Marshall, P. J., Hobson, M. P., Gull, S. F., & Bridle, S. L. 2002, MNRAS, 335, 1193B
Mortlock, D. J., Webster, R. L., & Francis, P. J. 1999, MNRAS, 309, 836
Peng, C. Y., Impey, C. D., Falco, E. E., et al. 1999, ApJ, 524, 572
Smith, G. P., Smail, I., Kneib, J.-P., et al. 2002a, MNRAS, 330, 1
Smith, G. P., Smail, I., Kneib, J.-P., et al. 2002b, MNRAS, 333, 16
Soucail, G., Kneib, J.-P., & Jaunsen, A. O., et al. 2001, A&A, 367, 741
Szeifert, T. 2002, FORS1 handbook
Spinrad, H., Dey, A., Stern, D., et al. 1997, ApJ, 484, 581
Stetson, P. 1987, PASP, 99, 191S
Thompson, D., Beckwith, S. V. W., Fockenbrock, R., et al. 1999, ApJ, 523, 100
Walsh, D., Carswell, R. F., & Weynmann, R. J. 1979, Nature, 279, 381